Journal Pre-proof

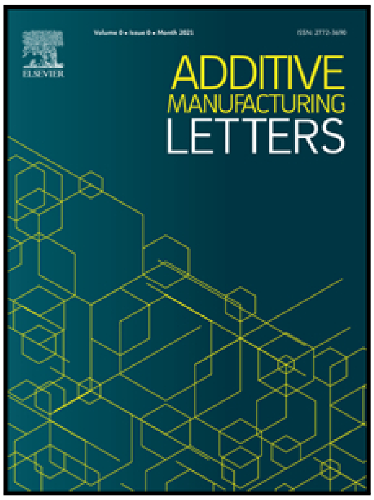

Onset of periodic oscillations as a precursor of a transition to pore-generating turbulence in laser melting

Saad A. Khairallah , Tao Sun , Brian J. Simonds

PII: S2772-3690(21)00002-5
DOI: https://doi.org/10.1016/j.addlet.2021.100002
Reference: ADDLET 100002

To appear in: *Additive Manufacturing Letters*

Received date: 24 May 2021
Revised date: 28 June 2021
Accepted date: 29 June 2021

Please cite this article as: Saad A. Khairallah , Tao Sun , Brian J. Simonds , Onset of periodic oscillations as a precursor of a transition to pore-generating turbulence in laser melting, *Additive Manufacturing Letters* (2021), doi: https://doi.org/10.1016/j.addlet.2021.100002

Highlights

- Narrowband oscillations of laser absorption precede multimodal oscillations
- Melt pool hydrodynamics drive oscillations when laser is stationary or scanned
- Simulations and X-ray imaging shows pore formation during multimodal oscillations

Onset of periodic oscillations as a precursor of a transition to pore-generating turbulence in laser melting

Saad A. Khairallah[1,*], Tao Sun[2], Brian J. Simonds[3,*]

[1]Lawrence Livermore National Laboratory, Livermore, CA 94550, USA

[2]Department of Materials Science and Engineering, University of Virginia, Charlottesville, VA 22904, USA

[3]Applied Physics Division, National Institute of Standards and Technology, Boulder, CO 80305, USA

[*]Corresponding Authors: khairallah1@llnl.gov, brian.simonds@nist.gov

Abstract

Laser melting technologies in welding and additive manufacturing, such as laser powder bed fusion, promises to revolutionize manufacturing. However, a challenge remains in preventing pore defects produced by melt pool instabilities, which degrade part quality. Using X-ray imaging synchronized with ultrahigh-speed (40 ns) absorption radiometry and coupled with high-fidelity simulations, we discovered that periodic oscillations in the melt pool's morphology existed prior to a transition to chaotic and pore-generating turbulence. Over-extension by recoil waves followed by surface-tension driven recession created temporary pores that persisted longer in a multimodal regime. This non-linear hydrodynamics exists in both shallow and deep melt pools, but most strongly affects the latter. Early prevention of this transition will help improve the quality of manufactured parts. This work demonstrates that remote sensing of these oscillations is possible by very high time resolution total light scattering measurements, which is more readily achievable in an industrial setting than 2-dimensional melt pool imaging.

Keywords: Additive Manufacturing, Keyhole, Porosity

1. Introduction

"Turbulence is the most important unsolved problem of classical physics"[1]. It is characterized by chaotic spatiotemporal fluctuations of state, such as pressure and velocity fields for a flowing fluid, and therefore it is challenging to understand in detail. Unfortunately, it is ubiquitous at all scales ranging from astronomical [2] to quantum [3]. Therefore, if neglected, it hinders the rapid development of new technologies [4,5]. Laser powder bed fusion additive manufacturing (LPBF AM), i.e. metal 3D printing, promises to revolutionize manufacturing by making complex parts economically and quickly [6]. However, it faces the challenge of minimizing melt pool turbulence [7], which in strong form appears as a highly fluctuating, or unstable, keyhole (deep and narrow melt pool). Keyholes arise in certain laser power-scan speed regimes [8,9] and generate undesirable pores that can ultimately lead to defective final parts [10].

During the LPBF printing process, a laser scans 2D patterns over a thin metal powder layer on a plate substrate. The laser creates a micrometer sized (~100 μm) melt pool that fuses the powder along the scan track. Upon solidification, a 2D layer of a part forms. Optimal process parameters create stable melt pools, and acceptable final part densification (> 99%). However, this is challenging to achieve. The fusion zone is dominated by a highly dynamic fluid flow that creates fluctuations in the amount of absorbed light. Spatter particles, resulting from gas entrainment and melt pool ejections [11–14], contribute additional instability to an already sensitive environment through a laser-spatter shadowing effect [7]. It is then easy to find conditions that exacerbate pore-generating melt pool turbulence, which add to the challenge of diagnosing and eliminating pores. Subsequently, these pores "lurk" beneath the surface, ready to seed a catastrophic mechanical failure.

Observations of keyhole dynamics have been greatly enhanced by recent applications of high brightness X-ray sources for high-speed X-ray imaging during laser processing. Some of these have reported keyhole fluctuations at higher laser irradiances and/or slower scan speeds [9,15] – process regimes that have been associated with pore defect formation. Here, we probed the keyhole fluctuation with ultra-high time resolution (25 MHz), uniquely afforded by the integration sphere technique. This allowed us to not only observe two distinct oscillatory regimes, but also resolve an abrupt shift between them in operando. This, combined with the X-ray imaging data and a high-fidelity multiphysics simulation, revealed the oscillatory melt pool dynamics in detail. The transition in keyhole fluctuation behaviors occurs over a narrow laser power range and is brief in time, which made it elusive to previous investigations. We found this transition in stationary laser beam exposures, as well as scanning conditions (unsteady and steady) found in LPBF AM or welding. This is encouraging since the small melt pool size and short time scales (~1 ns) create a challenge to practically monitor sub-surface turbulence. These oscillations can then be detected live by equipping 3D printers with backscattered light or probe beam sensors in order to rectify scanning conditions on-the-fly through feedback control to prevent pore-generating turbulence.

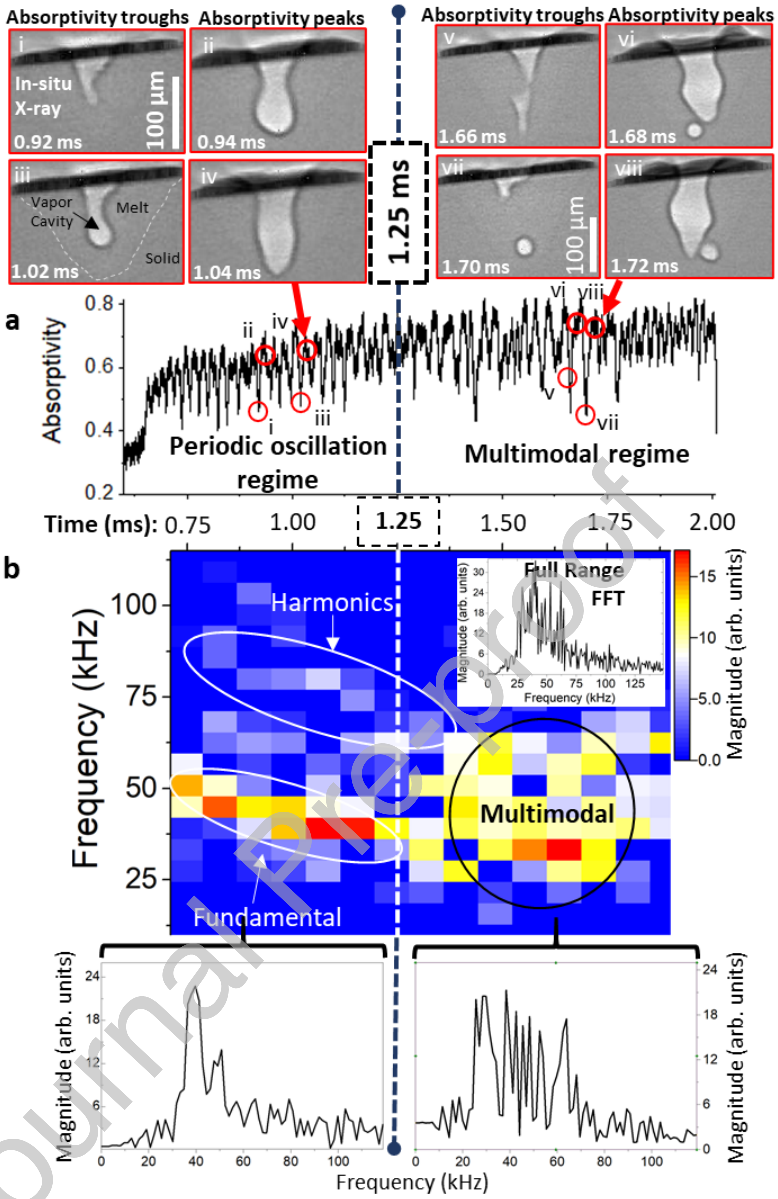

Figure 1. a Coupled X-ray imaging and integrating sphere radiometry correlate time resolved absorptivity data to melt-pool depression morphology for a stationary laser (108 W ± 1.4 W). The image features identified in **iii** generally apply to the other images as well. The transition to pore-generating turbulence is marked by the rise of a periodic oscillation. As turbulence evolves beyond 1.25 ms, temporary pores form frequently. **b** A histogram of fast-short time Fourier-transform spectrograph of absorptivity shows the decomposition of frequency over time. A narrowband frequency regime dominates early (0.75 ms -1.25 ms) with the fundamental (lowest periodic signal) frequency identified. A faint instantaneous second harmonic (double of the fundamental at a given time) is also present early. After ~1.25 ms, a multimodal regime defined by a broadband superposition of different frequency modes dominates. This signals the transition to pore-generating turbulence, where pores persist over multiple oscillations (Figure S2).

2. Experimental and Modeling Methods

We used a three-dimensional, high-fidelity multiphysics model to explain the physical mechanism behind the periodic oscillations. This thoroughly validated model [7,16,17] is coupled with high-speed X-ray imaging and integrating sphere radiometry to relate temporal absorptivity measurements in Ti-6Al-4V to the melt pool state (supplementary materials). The material's temperature-dependent absorptivity remains the main input assumption in modeling, and is a difficult quantity to measure [18–20], and therefore a calibrated, constant value is used [21,22]. Using ALE3D-4i [16], the current high-fidelity simulation model eliminates this approximation by coupling the thermal and hydrodynamic flow to a full laser ray tracing based on [23] while using temperature-dependent material properties. Hence, the absorptivity becomes an output that we can quantitatively compare with experimental integrating sphere results. We calculate the laser absorptivity (Abs.) as absorbed laser power divided by input laser power. The modeled Abs. can slightly deviate from the experiment due to simplifications made to amortize the computational expense of running a high-fidelity simulation. The laser is oriented at 7^{o} incident to the flat plate to match the experiment. However, the simulation box size is much smaller than the actual experiment. We also do not account for the vapor phase or production of weak plasma. A static laser will interact with the vapor plume longer, and thus will be more attenuated than the traveling laser case. Therefore, the heat dissipation process is different as well. We expect the simulation to produce a hotter melt pool, which affects the periodicity of the oscillations. However, the physical mechanisms driving the process will of course be the same.

The addition of powder particles on the surface will not change the physical mechanisms that created the oscillations. During the static scan or turnaround, the amount of energy focused on a single spot will cause immediate melting of powder on the surface. This increases the liquid volume at the surface close to the depression's opening. This can affect the frequency of the oscillations by increasing the period (decreasing the frequency), since a larger volume (inertia) has to move and oscillate. Indeed, in the experiment (Figure 1), we noticed the period increased with time, since the melt pool size kept growing from localized static heating with similar effects being seen previously [19,24,25].

We refer the reader to the thermophysical data (thermal conductivity, specific heat, density, volumetric expansion coefficient, latent heat of fusion and evaporation) previously published [26,27]. We note that the latent heat of evaporation is for pure titanium. The lack of latent heat of evaporation for Ti-6Al-4V introduces an uncertainty in the modeling of the balance of forces in the depression during the absorptivity rise and fall. The surface tension for Ti-6Al-4V follows the work of Aune et al.[28]

The high-speed X-ray imaging experiments were carried out at the 32-ID-B beamline of the Advanced Photon Source at Argonne National Laboratory with specific beamline details given in a previous publication [29]. The X-ray videos were captured at 50,000 frames per second with a 2.5 µs exposure time. The image analysis process has previously been fully described [30]. The Ti-6Al-4V samples were cut from NIST standard reference material (SRM 654b, Titanium-Based Alloy, 6Al-4V. National Institute of Standards and Technology: U.S. Department of Commerce, Gaithersburg, MD 2013) feedstock with wire electric discharge machining. These samples were 5 mm tall but only 300 µm thick to allow sufficient X-ray penetration. All sides were polished to achieve a smooth, specular finish. The laser used was a commercial fiber laser operating at 1070 nm wavelength, capable of a maximum of 500 W continuous laser power. The laser was focused at the sample surface to a measured spot size of 49.5 µm ± 5 µm ($1/e^2$).

The integrating sphere method as applied to laser processing has been fully described in a previous publication [19] and only a brief description is given here. A diagram of the experiment is given in the supplemental information Figure S1. A 3-inch inner diameter sphere was 3-dimensionally printed out of plastic, with a diffuse scattering inner surface generated with a combination of the native surface roughness and a spectrally flat coating. The focused high-power laser entered at a port at the top and the sample was placed an opposing port on the bottom. These were designed such that the laser hit the sample at a 7° angle of incidence, which ensured that the initially strong specular reflections were captured by the sphere. A photodiode was fiber-coupled to the sphere surface for detection, and a 1070 nm bandpass filter was placed in front of the photodiode sensor. The detection system was calibrated for absolute responsivity with samples of known specular and diffuse reflection, and it has a time resolution of 40 ns. The full uncertainty in the absorptivity measurement is 1.3 % (coverage factor of 1). The sphere and sample were positioned in the laser process chamber such that the X-ray beam transmitted through the sample, laser scan path, and laser poynting vector are all orthogonal [31].

Frequency analysis of the high-speed integrating sphere data was accomplished by short-time Fourier transform (STFT) analysis as presented in the spectrograms in Figures 1 and 3, and supplemental Figure S1, S2, and S4. These were computed over time regimes that exhibited oscillatory behavior. A 256 data point range with 128-point overlap was used for each time interval along with a Hanning window.

3. Results and Discussion

3.1 Transition to pore-generating turbulence

We first show the periodicity for a stationary, constant power laser (108 W ± 1.4 W; diameter = 49.5 μm ± 5 μm ($1/e^2$)) incident at 7^o to a Ti-6Al-4V flat plate. Ultra-high temporal resolution (40 ns) offered by integrating sphere radiometry system (ISR) [19] revealed oscillations in the time-dependent absorptivity (Figure 1). The periodic oscillations are stable for a short time (~250 μs) before transitioning to a multimodal regime. The observed frequencies were well below the Nyquist frequency (12.5 MHz) of our system ensuring that aliasing is avoided. Simultaneously obtained X-ray images [31] mark this transition with the frequent appearance and disappearance of temporary pores (See Supplemental Movie S1). We observed this transition over a narrow power range (96.6 W - 119 W), and the temporary pores persisted longer as the power or time increased (Figure S1).

We used a three-dimensional, high-fidelity multiphysics model to explain the physical mechanism behind these periodic oscillations. The simulation shows that the periodic variations in the depression and the top surface melt are synchronized with the periodic absorptivity oscillations (Figure 2a-b; Movie S2) and reveals how the oscillation mechanism is driven by a tug-of-war between two opposing surface forces: surface tension and recoil pressure. The simulation figures (Figure 2c-e) are complemented with select high-speed X-ray images and ISR plots with red circular markers to relate temporal absorptivity measurements to the melt pool's depression morphology.

The absorptivity is at its peak in (Figure 2c, 406 μs) because a maximally wide and extended depression encourages more multiple laser reflections (energy depositions). In this metastable state, the absorbed energy density (energy per area) is not uniform. Cold spots (green-yellow pseudo-colors) close to the top of the depression indicate a dominant surface tension force that is closing the top and pulling surface flow from the bottom hot to top cold regions via the Marangoni effect: The depression is in recession at 410 μs. The absorptivity hits a minimum when the top of the depression has narrowed into a tight channel (Figure 2d, 416 μs) that limits further laser light from penetrating the depression and keeping the absorptivity high due to multiple reflections . However, the absorptivity starts to rise 2 ms shortly after (Figure 2d, 418 μs) when a recoil wave develops instantaneously at the top, narrow channel and travels quickly to the bottom at ~20 m/s (Supplemental Movie S2). The wave appears when the surface tension, which has almost vanished over the boiling top narrow channel, is suddenly overtaken by an exponentially rising recoil pressure (exponential in temperature). The depression widens and elongates, allowing more light to perform multiple reflections. The narrow channel in Figure 2d, 420 μs breaks the depression into hot and cold halves. The dynamics in the cold half is dominated by the surface tension force which acts to decrease the surface energy by decreasing the surface area, which is achieved by a spherical pore geometry. The velocity vector field in the bottom half is pointing inwards, towards the inside of the depression, which indicates that the surface tension is pulling the surface inward in order to close the channel. The bottom half may break away from the top half (Figure 2d, 422 ms), hence creating a temporary pore. As the recoil wave travels further down, it forces any temporary pore at the bottom to merge with the extending depression (Figure 2d, 427 ms). The lack of inertia resistance inside the pore, causes the wave to converge sharply at the bottom, creating a pointed end (Figure 2e). The resulting over-extended depression signals the start of a new cycle. Along with these keyhole hydrodynamics, the top surface melt pool oscillates in-sync with absorptivity as the top views in Figure 2c-e and Supplemental Movie S2 show periodic outward and inward motion.

It should be noted that melt pool oscillations have been observed by many groups first in welding and later in AM with a good literature review found in [32]. The mechanisms of the oscillation, as well as the frequency, is related to processing conditions and melt pool dimensions. In other words, not all oscillations result from the same phenomenon and the measurements and analysis here are restricted to keyhole cavity oscillations under conditions relevant to LPBF AM.

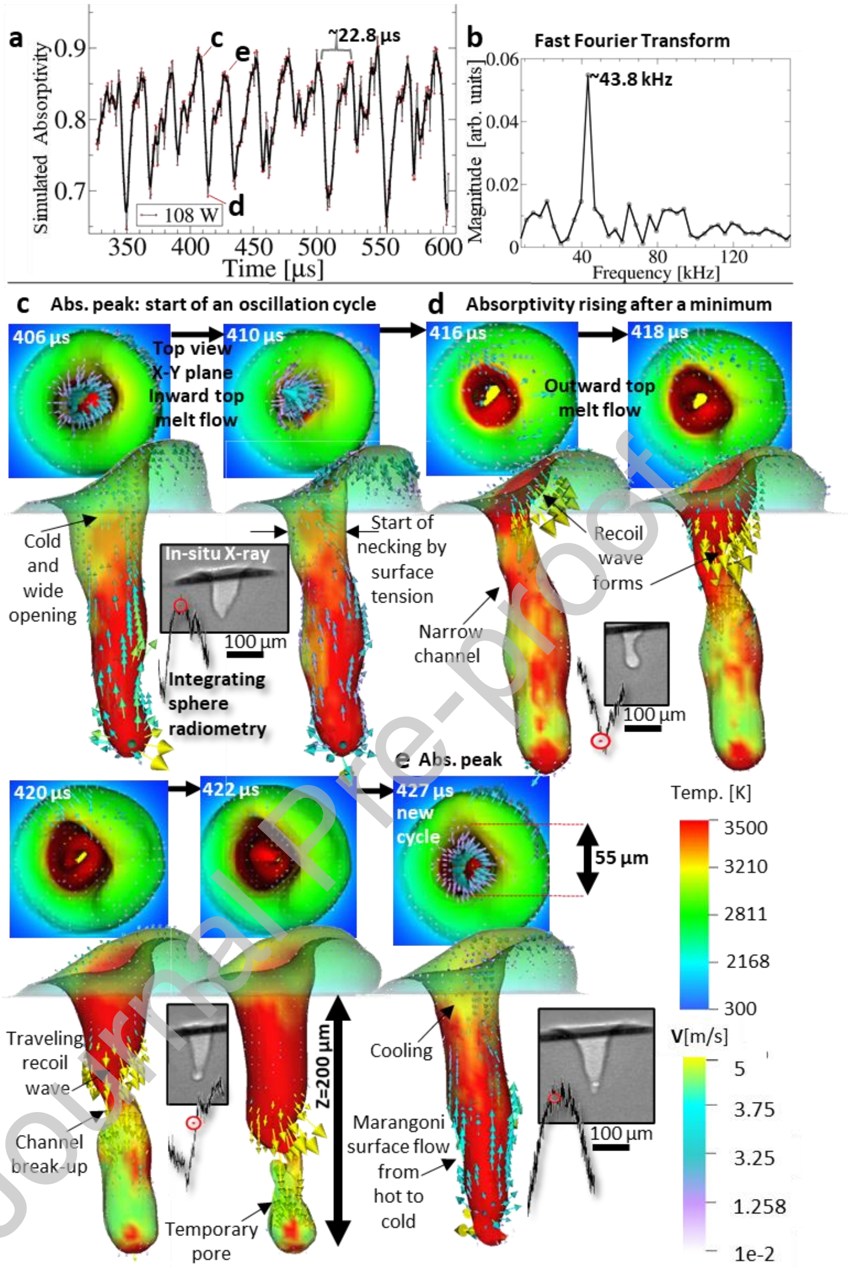

Figure 2. **a** Simulated absorptivity (Abs.) for a stationary constant laser power (108 W). The letters **c-e** cover variations in the depression's morphology during a single period covered in panels **c-e**. **b** A peak in the Fourier-transform of **a** indicates a periodic signal. **c** Absorption is at its peak for a maximally extended and widely open depression. Later, the surface tension creates a necking on top, which closes the opening and causes a collapse in absorptivity **d** A recoil wave forms and extends the depression and merges it with a temporary pore that previously broke away at the bottom. The traveling wave increases the absorptivity. **e** The cycle starts anew with a cooling on top. The velocity vector field V[m/s] is applied to the depression's surface (semi-transparent) and the color scale is maxed at 5 m/s for visual clarity (Supplemental Movie S2).

3.2 Periodicity during raster scan

The periodic interplay between recoil pressure and surface tension is not limited to a stationary constant laser power. We observed oscillations during steady and complex (non-steady) laser scans (Figure 3, Supplementary Figure S4, Supplemental Movies S3 and S4). Figure 3a subdivides the absorptivity of a single laser track into three regions. As the laser power ramps up, few oscillations (~25 kHz) set in, signaling initial turbulence and a micro-pore (~3 μm at 244 μs, Supplemental Movie S3). However, the oscillations fade (damped oscillations) as the scan enters a steady state and no further pores are generated. During these oscillations, the absorptivity maxima occurred when the back of the depression formed an inverted "S" shape (bottom depression extends backward) that extended and receded repeatedly (Figure 3b, 319 ms - 402 ms, Supplemental Movie S3) under the action of surface tension and recoil pressure. Similar morphological variations and damped turbulence at low frequency (25 kHz) are observed experimentally for a steady laser scan at 261 W ± 3 W and 700 mm/s (Figure 3c, Supplemental Movie S4). Additional experimental evidence for steady state oscillations was found in reference [9] in the X-ray movie S9 (84 W, 200 mm/s, laser spot ~100 μm). Here, vertical fluctuations resolved at 20 μs time intervals, appear to be periodic and produce only temporary pores (compare oscillations to our Supplemental Movie S1). By slightly increasing the energy density, in Movie S8 [9] (84 W, 150 mm/s), more temporary pores and some frozen ones appeared, which signaled a transition to the multimodal regime.

As the laser decelerated in order to reverse direction at the turn-around location (Figure 3d), it behaved as a quasi-stationary beam. The high fundamental frequency of ~50 kHz, similar to Figure 1 and 2, signaled a transition to turbulence and temporary pore formation. Just as the laser accelerated to the left, exiting the turn-around location, Figure 3e reveals that the temporary pores were caught by the moving solid-liquid front and therefore froze in place. A lower power [7] or slower acceleration at the turn-around exit can prevent this. This transition in turbulence explains why pores appear after the turn-around location [33] and agrees with [9] as pores may form at the tip of the depression.

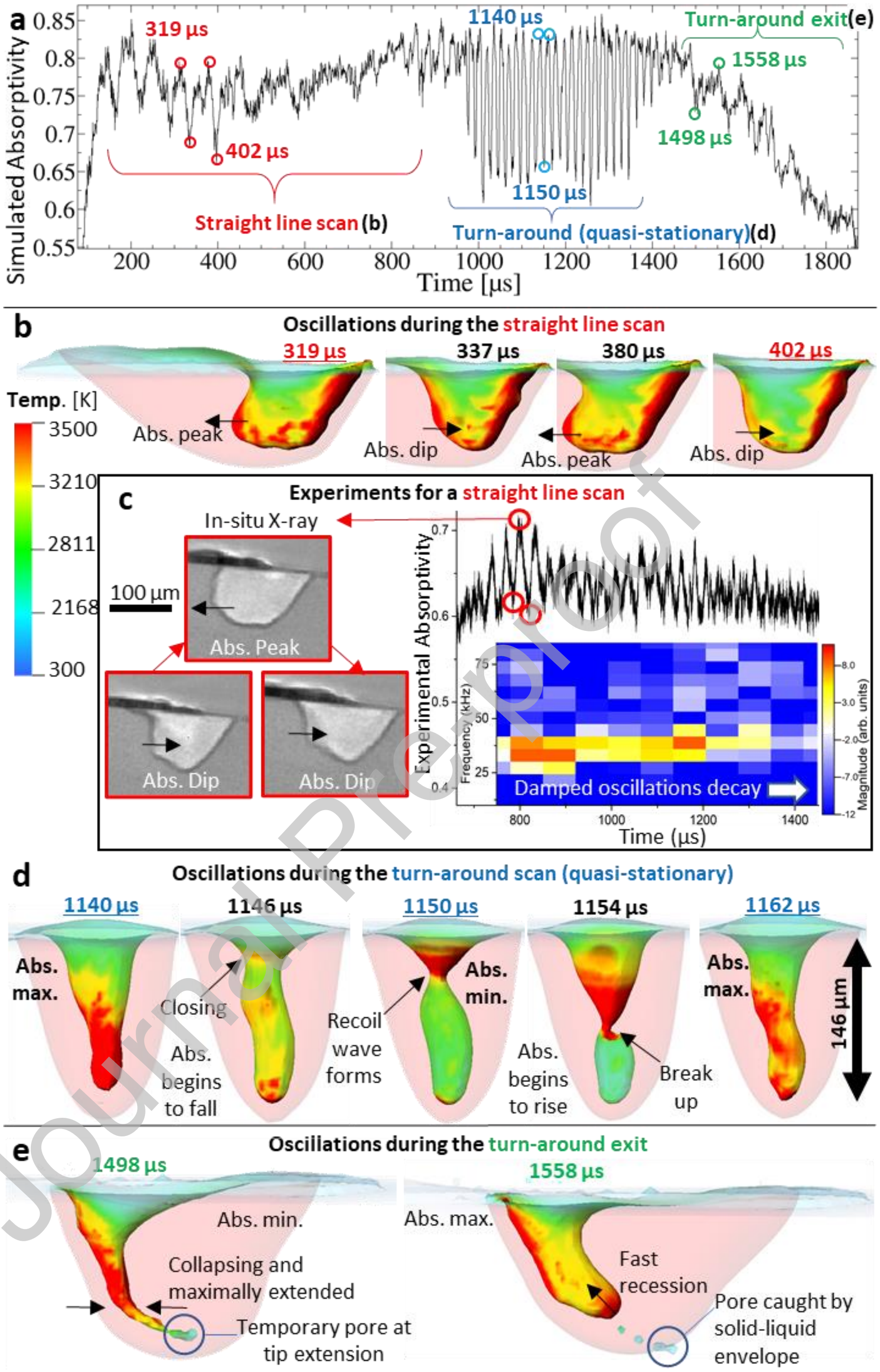

Figure 3. a Single laser track simulation shows oscillations in transient melt pool states. The power and scan speed vary along the track according to supplementary Figure S4. **b** Damped low frequency oscillation (25 kHz), as the melt pool starts to travel to the right, indicates a decay in turbulence and no pores. The black arrows indicate oscillatory motion. **c** Coupled in-situ X-ray and integrating sphere (ISR) experiments conducted at constant power and steady state show damped oscillations (25 kHz) that are morphologically consistent with **b**. No pores are detected as the damped oscillations disappear over

time (Supplementary Figure S2). **d** The laser is almost stationary as it reverses scan direction at the turn-around. High frequency periodic oscillation (period ~20 μs, 50 kHz), signals turbulence and temporary pores form. **e** As the laser exits the turn and moves back to the left, a temporary pore is caught by the solid-liquid melt pool boundary (red) and freezes (Supplemental Movies S3-4).

4. Conclusion

Pores are a persistent nuisance to laser melting technologies. We have discovered that pore-generating turbulence is preceded by narrow frequency periodic oscillations in the melt pool depression (liquid-gas interface) that is readily detected by ultrahigh-speed backscattered laser light measurements. Therefore, such real-time monitoring for melt pool oscillatory extensions and recessions, as power and/or scan speed are varied or maintained fixed, can potentially prevent pores as oscillations foretell the arrival of pore-generating turbulence. The addition of powder (LPBF) may randomly introduce additional transient perturbations caused by large spatter-laser interactions [7], making high-frequency, real-time sensing more of an imperative. Ultimately, these sensing strategies must make use of high-temporal resolution in situ detection techniques that produce, low-dimensional, easy to interpret data, and that can be integrated into an industrial LPBF instrument. A backscattered laser light-based technique that gives qualitatively similar information to ISR could be one such technique. Deploying smart rectification strategies will enable smarter process control strategies, and ultimately more reliable final parts.

Funding

Work performed under auspices of U.S. Department of Energy by Lawrence Livermore National Laboratory contract DE-AC52-07NA27344. WTE-CMD-CRADA-TC02303/WSC-ASC-IC-AM-ALE3D. This research used resources from the Advanced Photon Source, a U.S. Department of Energy (DOE) Office of Science User Facility operated for the DOE Office of Science by Argonne National Laboratory under Contract No. DE-AC02-06CH11357. Release LLNL-JRNL-819346;

Declaration of interests

☒ The authors declare that they have no known competing financial interests or personal relationships that could have appeared to influence the work reported in this paper.

Acknowledgements
R. Ferencz, M. J. Matthews (support), A. A. Martin (discussion), C. Zhao, N. D. Parab (experimental help). N. Derimow (optical images), P. Williams, B. Lane (feedback).

References

[1] R.P. Feynman, R.B. Leighton, M. Sands, The Feynman Lectures on Physics, Addison-Wesley, 1964.

[2] V.M. Canuto, J. Christensen-Dalsgaard, TURBULENCE IN ASTROPHYSICS: Stars, Annu. Rev. Fluid Mech. 30 (1998) 167–198. https://doi.org/10.1146/annurev.fluid.30.1.167.

[3] C.F. Barenghi, L. Skrbek, K.R. Sreenivasan, Introduction to quantum turbulence, Proc. Natl. Acad. Sci. 111 (2014) 4647 LP – 4652. https://doi.org/10.1073/pnas.1400033111.

[4] S. Davidovits, N.J. Fisch, Sudden Viscous Dissipation of Compressing Turbulence, Phys. Rev. Lett. 116 (2016) 105004. https://doi.org/10.1103/PhysRevLett.116.105004.

[5] P. Veers, K. Dykes, E. Lantz, S. Barth, C.L. Bottasso, O. Carlson, A. Clifton, J. Green, P. Green, H. Holttinen, D. Laird, V. Lehtomäki, J.K. Lundquist, J. Manwell, M. Marquis, C. Meneveau, P. Moriarty, X. Munduate, M. Muskulus, J. Naughton, L. Pao, J. Paquette, J. Peinke, A. Robertson, J. Sanz Rodrigo, A.M. Sempreviva, J.C. Smith, A. Tuohy, R. Wiser, Grand challenges in the science of wind energy, Science (80-.). 366 (2019) eaau2027. https://doi.org/10.1126/science.aau2027.

[6] T. Wohlers, 3D printing and additive manufacturing state of the industry, Wohlers Associates, 2018.

[7] S.A. Khairallah, A.A. Martin, J.R.I. Lee, G. Guss, N.P. Calta, J.A. Hammons, M.H. Nielsen, K. Chaput, E. Schwalbach, M.N. Shah, M.G. Chapman, T.M. Willey, A.M. Rubenchik, A.T. Anderson, Y.M. Wang, M.J. Matthews, W.E. King, Controlling interdependent meso-nanosecond dynamics and defect generation in metal 3D printing, Science (80-.). 368 (2020) 660–665.

[8] R. Cunningham, C. Zhao, N. Parab, C. Kantzos, J. Pauza, K. Fezzaa, T. Sun, A.D. Rollett, Keyhole threshold and morphology in laser melting revealed by ultrahigh-speed x-ray imaging, Science (80-.). 363 (2019) 849–852. https://doi.org/10.1126/science.aav4687.

[9] C. Zhao, N.D. Parab, X. Li, K. Fezzaa, W. Tan, A.D. Rollett, T. Sun, Critical instability at moving keyhole tip generates porosity in laser melting, Science (80-.). 370 (2020) 1080 LP – 1086. https://doi.org/10.1126/science.abd1587.

[10] T. DebRoy, H.L. Wei, J.S. Zuback, T. Mukherjee, J.W. Elmer, J.O. Milewski, A.M. Beese, A. Wilson-Heid, A. De, W. Zhang, Additive manufacturing of metallic components – Process, structure and properties, Prog. Mater. Sci. 92 (2018) 112–224. https://doi.org/10.1016/j.pmatsci.2017.10.001.

[11] M.J. Matthews, G. Guss, S.A. Khairallah, A.M. Rubenchik, P.J. Depond, W.E. King, Denudation of metal powder layers in laser powder bed fusion processes, Acta Mater. 114 (2016) 33–42. https://doi.org/10.1016/j.actamat.2016.05.017.

[12] C. Zhao, K. Fezzaa, R.W. Cunningham, H. Wen, F. De Carlo, L. Chen, A.D. Rollett, T. Sun, Real-time monitoring of laser powder bed fusion process using high-speed X-ray imaging and diffraction, Sci. Rep. 7 (2017) 3602. https://doi.org/10.1038/s41598-017-03761-2.

[13] P. Bidare, I. Bitharas, R.M. Ward, M.M. Attallah, A.J. Moore, Fluid and particle dynamics in laser powder bed fusion, Acta Mater. 142 (2018) 107–120. https://doi.org/10.1016/j.actamat.2017.09.051.

[14] C.L.A. Leung, S. Marussi, R.C. Atwood, M. Towrie, P.J. Withers, P.D. Lee, In situ X-ray imaging of defect and molten pool dynamics in laser additive manufacturing, Nat. Commun. 9 (2018) 1355. https://doi.org/10.1038/s41467-018-03734-7.

[15] Y. Chen, S.J. Clark, C.L.A. Leung, L. Sinclair, S. Marussi, M.P. Olbinado, E. Boller, A. Rack, I. Todd, P.D. Lee, In-situ Synchrotron imaging of keyhole mode multi-layer laser powder bed fusion additive manufacturing, Appl. Mater. Today. 20 (2020) 100650. https://doi.org/10.1016/j.apmt.2020.100650.

[16] ALE3D for industry, (2018). https://ale3d4i.llnl.gov.

[17] J. Ye, S.A. Khairallah, A.M. Rubenchik, M.F. Crumb, G. Guss, J. Belak, M.J. Matthews, Energy Coupling Mechanisms and Scaling Behavior Associated with Laser Powder Bed Fusion Additive Manufacturing, Adv. Eng. Mater. 1900185 (2019) 1900185. https://doi.org/10.1002/adem.201900185.

[18] J. Trapp, A.M. Rubenchik, G. Guss, M.J. Matthews, In situ absorptivity measurements of metallic powders during laser powder-bed fusion additive manufacturing, Appl. Mater. Today. 9 (2017) 341–349. https://doi.org/10.1016/j.apmt.2017.08.006.

[19] B.J. Simonds, J. Sowards, J. Hadler, E. Pfeif, B. Wilthan, J. Tanner, P. Williams, J. Lehman, Time-resolved Absorptance and Melt Pool Dynamics during Intense Laser Irradiation of Metal, Phys. Rev. Appl. 10 (2018) 044061–14. https://doi.org/10.1103/PhysRevApplied.10.044061.

[20] B.J. Simonds, E.J. Garboczi, T.A. Palmer, P.A. Williams, Dynamic laser absorptance measured in a geometrically characterized stainless-steel powder layer, Phys. Rev. Appl. 13 (2020) 024057.

[21] S.A. Khairallah, A. Anderson, Mesoscopic simulation model of selective laser melting of stainless steel powder, J. Mater. Process. Technol. 214 (2014) 2627–2636. https://doi.org/https://doi.org/10.1016/j.jmatprotec.2014.06.001.

[22] S.A. Khairallah, A.T. Anderson, A. Rubenchik, W.E. King, Laser powder-bed fusion additive manufacturing: Physics of complex melt flow and formation mechanisms of pores, spatter, and denudation zones, Acta Mater. 108 (2016) 36–45. https://doi.org/10.1016/j.actamat.2016.02.014.

[23] T.B. Kaiser, Laser ray tracing and power deposition on an unstructured three-dimensional grid, Phys. Rev. E. 61 (2000) 895–905. https://doi.org/10.1103/PhysRevE.61.895.

[24] T.R. Allen, W. Huang, J. Tanner, W. Tan, J.M. Fraser, B.J. Simonds, Energy-Coupling Mechanisms Revealed through Simultaneous Keyhole Depth and Absorptance Measurements during Laser-Metal Processing, Phys. Rev. Appl. 13 (2020) 064070.

[25] T.R. Allen, B.J. Simonds, J.R. Tanner, J.M. Fraser, Simultaneous in operando monitoring of keyhole depth and absorptance in laser processing of AISI 316 stainless steel at 200 kHz, Procedia CIRP. 94 (2020) 419–424. https://doi.org/10.1016/j.procir.2020.09.157.

[26] K.C. Mills, Recommended Values of Thermophysical Properties for Selected Commercial Alloys, Woodhead Publishing Ltd., Cambridge, England, 2002.

[27] T. Mukherjee, H.L. Wei, A. De, T. DebRoy, Heat and fluid flow in additive

manufacturing – Part II: Powder bed fusion of stainless steel, and titanium, nickel and aluminum base alloys, Comput. Mater. Sci. 150 (2018) 369–380. https://doi.org/https://doi.org/10.1016/j.commatsci.2018.04.027.

[28] R. Aune, L. Battezzati, R. Brooks, I. Egry, H.-J. Fecht, J.-P. Garandet, K.C. Mills, A. Passerone, P.N. Quested, E. Ricci, S. Schneider, S. Seetharaman, R.K. Wunderlich, B. Vinet, Surface tension and viscosity of industrial alloys from parabolic flight experiments — Results of theThermoLab project, Microgravity - Sci. Technol. 16 (2005) 11–14. https://doi.org/10.1007/BF02945937.

[29] N.D. Parab, L.I. Escano, K. Fezzaa, W. Everhart, A.D. Rollett, L. Chen, T. Sun, Ultrafast X-ray imaging of laser – metal additive manufacturing processes, J. Synchrotron Radiat. 25 (2018) 1467–1477. https://doi.org/10.1107/S1600577518009554.

[30] B.J. Simonds, J. Tanner, A. Artusio-Glimpse, P.A. Williams, N. Parab, C. Zhao, T. Sun, Simultaneous high-speed x-ray transmission imaging and absolute dynamic absorptance measurements during high-power laser-metal processing, in: Procedia CIRP, 2020. https://doi.org/10.1016/j.procir.2020.09.135.

[31] B. Simonds, J. Tanner, A. Artusio-Glimpse, P.A. Williams, N. Parab, C. Zhao, T. Sun, The causal relationship between melt pool geometry and energy absorption measured in real time during laser-based manufacturing, Appl. Mater. Today. 23 (2021) 101049. https://doi.org/https://doi.org/10.1016/j.apmt.2021.101049.

[32] L. Caprio, A.G. Demir, B. Previtali, Observing molten pool surface oscillations during keyhole processing in laser powder bed fusion as a novel method to estimate the penetration depth, Addit. Manuf. (2020) 101470.

https://doi.org/10.1016/j.addma.2020.101470.

[33] A.A. Martin, N.P. Calta, S.A. Khairallah, J. Wang, P.J. Depond, A.Y. Fong, V. Thampy, G.M. Guss, A.M. Kiss, K.H. Stone, C.J. Tassone, J. Nelson Weker, M.F. Toney, T. van Buuren, M.J. Matthews, Dynamics of pore formation during laser powder bed fusion additive manufacturing, Nat. Commun. 10 (2019) 1987. https://doi.org/10.1038/s41467-019-10009-2.

Graphical abstract